International Journal of Hydrogen Energy 148 (2025) 149833

Contents lists available at ScienceDirect

International Journal of Hydrogen Energy

journal homepage: www.elsevier.com/locate/he

Influence of stacking fault energy and hydrogen on deformation mechanisms in high Mn austenitic steels during *in-situ* tensile testing

Yuran Kong [a], Pawan Kathayat [a], Alec Williamson [a], Donald W. Brown [b], Samantha K. Lawrence [b], Bjørn Clausen [b], Sven C. Vogel [b], Joseph A. Ronevich [c], Chris W. San Marchi [c], Lucas Ravkov [d], Levente Balogh [d], John G. Speer [a], Kip O. Findley [a], Lawrence Cho [a,*]

[a] *Advanced Steel Processing and Products Research Center (ASPPRC), Colorado School of Mines, Golden, CO, 80401, USA*
[b] *Los Alamos National Laboratory, Los Alamos, NM, 87545, USA*
[c] *Sandia National Laboratories, Livermore, CA, 94550, USA*
[d] *Queens University, Kingston, ON, K7L 3N6, Canada*

ARTICLE INFO

Keywords:
High Mn austenitic steel
Hydrogen embrittlement
Stacking fault energy
Neutron diffraction

ABSTRACT

High Mn austenitic steels are considered an economical alloy system for hydrogen storage and transport applications. This study used stacking fault energy (SFE) as a design parameter to achieve hydrogen embrittlement (HE)-resistant high Mn austenitic alloys. The role of hydrogen on the deformation mechanisms of low (29 mJ/m^2) and high SFE (49 mJ/m^2) alloys was evaluated through *in-situ* neutron diffraction during tensile loading. Hydrogen-precharging increased yield strength, partly due to hydrogen-induced lattice distortion (*i.e.*, solute strengthening). Hydrogen accelerated the increase in defect density, including dislocations and stacking faults. The formation of planar deformation structures (twins and stacking faults), relative to dislocations, plays a critical role in promoting hydrogen-assisted fracture. The stacking fault frequency parameter obtained from neutron diffraction quantifies planar deformation tendencies, correlated with HE sensitivity. The higher SFE alloy exhibited greater resistance to HE, associated with the reduced propensity to form stacking faults and twins upon deformation in the hydrogen-precharged condition.

1. Introduction

To reduce costs associated with hydrogen (H) transport and fueling infrastructure, it is critical to decrease the cost of alloys used for these applications. High Mn austenitic steels may be an economical alternative to commonly utilized austenitic stainless steels with high content of expensive alloying elements (e.g. nickel), provided that these steels can demonstrate high resistance to embrittlement under extreme gaseous H charging environments.

Austenite stacking fault energy (SFE) has been proposed as a critical design parameter for achieving HE resistance. For example, Gibbs et al. [1] reported that an SFE of at least 40 mJ/m^2 is required to achieve H embrittlement (HE) resistance in austenitic alloys relying on both Ni and Mn stabilization of the austenite. Gibbs et al. [1] and others [2,3] attributed the influence of SFE to its effect on deformation mechanisms, which are closely linked with HE sensitivity. In austenitic alloys, H promotes localized deformation and the formation of planar deformation structures, such as twins and ε-martensite, which are detrimental to HE resistance [3]. A higher SFE reduces the likelihood of deformation-induced twinning or martensitic transformations and thus, increases HE resistance. In support of this mechanism, previous studies have shown that deformation twin boundaries and their interactions with grain boundaries are critical sites for H-induced cracking in austenitic steels [4–7]. While the role of H in promoting localized deformation is well-established [8,9], systematic and quantitative analysis of interactions between H and defects is required to formalize the correlations between SFE, deformation mechanisms, and HE mechanisms in austenitic alloys, including high Mn steels, designed for H service applications.

The current study focuses on the deformation mechanisms and HE resistance of two high Mn austenitic steels, designed to exhibit different SFE values: one below the proposed threshold (approximately 29 mJ/

* Corresponding author.
E-mail address: lcho@mines.edu (L. Cho).

https://doi.org/10.1016/j.ijhydene.2025.06.023
Received 9 April 2025; Received in revised form 29 May 2025; Accepted 2 June 2025
Available online 20 June 2025

m^2) and the other above it (approximately 49 mJ/m^2). The deformation and HE mechanisms in these two alloys are compared in non-charged and H-precharged states using electron backscatter diffraction (EBSD) and *in-situ* neutron diffraction techniques, established in recent work by the present authors [10].

2. Experimental

The two austenitic high Mn alloys were received as hot-rolled plates, and their compositions and corresponding SFE values are shown in Table 1. Note that the details of the prior processing history, including hot rolling parameters, are proprietary. In this paper, the alloys with low (29 mJ/m^2) and high SFE (49 mJ/m^2) are labeled LSFE and HSFE, respectively. The basis of the thermodynamic model used to estimate the intrinsic SFE is given in Equation (1):

$$\gamma_{SFE} = 2\rho\,(\Delta G_{\gamma\rightarrow\varepsilon}) + 2\sigma, \qquad \text{Eq. 1}$$

where γ_{SFE} is the intrinsic SFE, $\Delta G_{\gamma\rightarrow\varepsilon}$ is the Gibbs free energy of austenite (γ) to ε-martensite phase transformation, σ is the interfacial energy per unit area of the phase boundary, and ρ is the molar surface density of the closed-packed plane (i.e. {111} plane for austenite). The Gibbs free energy term, $\Delta G_{\gamma\rightarrow\varepsilon}$, contains the composition dependence of SFE through a chemical driving force term, which is composed of both individual element contributions to driving force as well as the interaction between elements. An interfacial energy value of 8 mJ/m^2 was used for σ, as reported by Gibbs et al. [1] and Saeed-Akbari et al. [11]. Further details regarding the computation of $\Delta G_{\gamma\rightarrow\varepsilon}$ and ρ can be found in the M.S. thesis by Kathayat [12].

The tensile properties of the high Mn steels in an ambient environment (non-charged condition) were measured using subsize smooth tensile specimens with a gauge length of 25.4 mm and a gauge diameter of 3.8 mm. Tensile testing was performed at a constant displacement rate of 0.0127 mm/s. The microstructures of the tensile specimens were investigated using EBSD before and after testing. Before the analysis, the specimens were mounted, mechanically ground, and polished with a final polishing step using a vibratory polisher and colloidal silica with a particle size of 0.02 μm. The samples were analyzed in a field emission-scanning electron microscope (SEM) equipped with EBSD.

The *in-situ* deformation behavior of the alloys in the as-received, non-charged conditions and H-precharged conditions was characterized through neutron diffraction measurements using the Spectrometer for Materials Research at Temperature and Stress (SMARTS) neutron diffractometer at the Los Alamos Neutron Science Center (LANSCE). For *in-situ* neutron diffraction measurements during tensile loading, a round bar-type tensile specimen was mounted in the SMARTS instrument such that the loading direction was oriented 135° with respect to the direction of the incident beam. This configuration allowed for simultaneous measurement of the longitudinal and transverse strain components, obtained from −90° and 90° detector banks, respectively. The diameter of the specimen gauge section was 6.35 mm. A 12.5 mm-gauge length extensometer was used to measure displacement during testing. The *in-situ* tensile test was interrupted while the neutron diffraction data were recorded under load control in the elastic regime, followed by displacement control from the elastic-plastic transition through the plastic regime, using a displacement rate of 0.005 mm/s. Further details of the specimen geometry and testing methodology can be found in another publication [10]. Thermal H pre-charging at a temperature of 300 °C was conducted in gaseous H at a pressure of ∼138 MPa for 20 days. The H-precharged, tensile specimens were delivered to the LANSCE in a cryogenic package involving dry ice and stored cryogenically at −55 °C before the neutron diffraction measurement to minimize H desorption from the samples before analysis.

Table 1
Chemical compositions (wt pct) and estimated SFE of two high Mn austenitic steels used for the current study.

Alloy	Fe	C	Mn	Cr	Al	Ni	SFE ($mJ\cdot m^{-2}$)
LSFE	Bal.	0.24	30.0	2.73	–	–	29
HSFE	Bal.	0.25	30.4	2.71	1.75	3.0	49

3. Results and discussion

Fig. 1 shows EBSD inverse pole figure (IPF) maps and corresponding grain size distribution histograms for the initial microstructures of the LSFE and HSFE high Mn austenitic steels, i.e. prior to tensile straining. The EBSD analysis indicated that the area-weighted average grain sizes for the LSFE and HSFE alloys were 21.8 μm and 33.2 μm, respectively. Both alloys exhibited a mixture of coarse, elongated grains and equiaxed grains. In particular, the HSFE alloy displayed a less uniform grain size distribution, with the histogram indicating a bimodal grain structure.

Fig. 2(a) shows a calculated SFE map for an Fe-0.25C–30Mn-xAl-yNi system, and the nominal alloy compositions and calculated SFE values for both the HSFE and LSFE alloys are marked on the map. This SFE map indicates that the HSFE alloy exhibits a higher SFE than the LSFE alloy, as SFE increases with increasing Ni and Al contents. Fig. 2(b) and (c) show the deformed microstructures of the HSFE and LSFE alloys, respectively, tested in the non-charged condition. The LSFE (∼29 mJ/m^2) alloy exhibited extensive straight or planar features, such as deformation twins and stacking faults, consistent with an SFE regime (15–45 mJ/m^2 [13]) that promotes deformation twinning. In contrast, the presence of planar features was limited in the deformed HSFE microstructure, as its SFE (∼49 mJ/m^2) lies within a regime (>45 mJ/m^2 [13]) that favors dislocation glide and less planar slip. Table 2 and Supplementary Fig. S1 present the notch tensile strength (NTS) for the alloys tested in both air and electrochemical H charging environments, indicating that compared to the LSFE alloy, the HSFE alloy demonstrates higher HE resistance, reflected in a smaller reduction in NTS in the H charging environment [12,14]. Fractographic analysis of the tested specimens (Supplementary Fig. S1) supports this finding; the LSFE alloy showed transgranular brittle fracture, including H-induced secondary cracks, while the HSFE alloy exhibited microvoid coalescence, consistent with the insignificant NTS degradation.

Fig. 3(a)and (b) show true stress-strain curves for the two alloys tested under non-charged and H-precharged conditions. The vertical segments in the curves, marked with grey arrowheads, illustrate stress relaxation during holds for neutron diffraction measurements. For both alloys in the non-charged condition, the tests were interrupted before reaching the ultimate tensile strength (UTS), i.e. these specimens did not fracture. In contrast, the H-precharged specimens fractured due to HE prior to reaching UTS. The H-precharged LSFE and HSFE alloys fractured at true strains of 0.12 and 0.32, respectively, highlighting the superior HE resistance of the HSFE alloy as expected due to its higher SFE. These results are consistent with the HE tests conducted with electrochemical H charging (Table 2), which showed a smaller H-induced loss in NTS for the HSFE alloy.

For both alloys, H precharging resulted in strengthening, and this effect was greater for the LSFE alloy (Fig. 3(a) and (b)). Fig. 4(a) and (b) show the evolution of lattice strains during testing in non-charged and H-precharged conditions of the two alloys. The H effect on the lattice strains is consistent with the trends observed in the stress-strain curves, suggesting that H-induced strengthening is primarily associated with H solid solution strengthening resulting from H-induced lattice distortion. The LSFE alloy exhibited significantly higher lattice strain for the H-precharged condition. The HSFE alloy similarly exhibited an increase in lattice strain at a true strain range of 0–0.03. At a true strain higher than 0.045, the non-charged and H-precharged conditions exhibited similar lattice strains for the HSFE alloy, which is a different behavior from the LSFE alloy.

Fig. 5 shows the influence of alloying and H charging on the austenite lattice parameters for the LSFE and HSFE alloys in the non-deformed conditions. Overall, regardless of the axial or transverse orientation

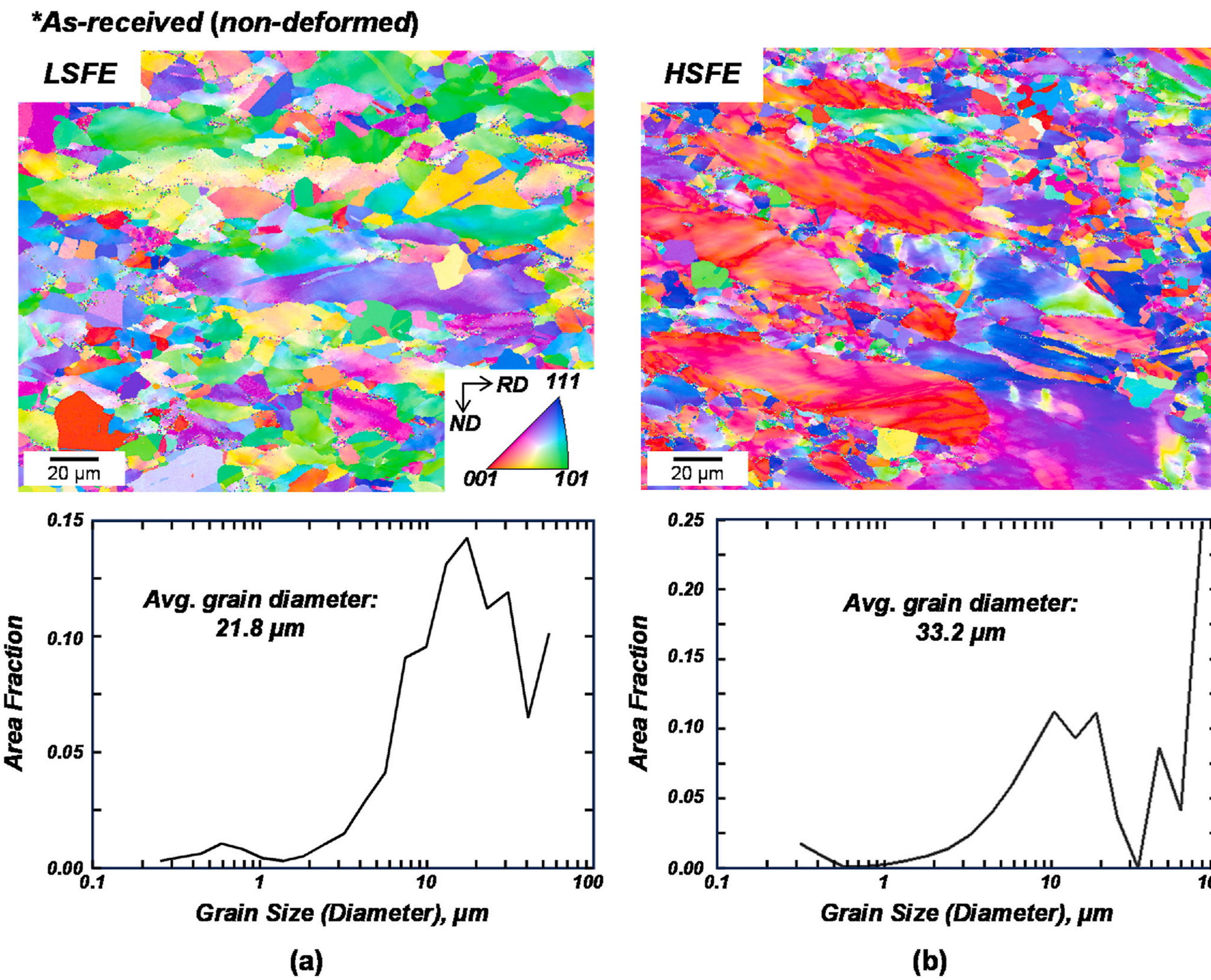

Fig. 1. EBSD IPF maps (top) and histogram of grain size distribution, i.e. area fraction versus grain diameter, (bottom) for the as-received microstructures of (a) the LSFE and (b) HSFE high Mn austenitic steels.

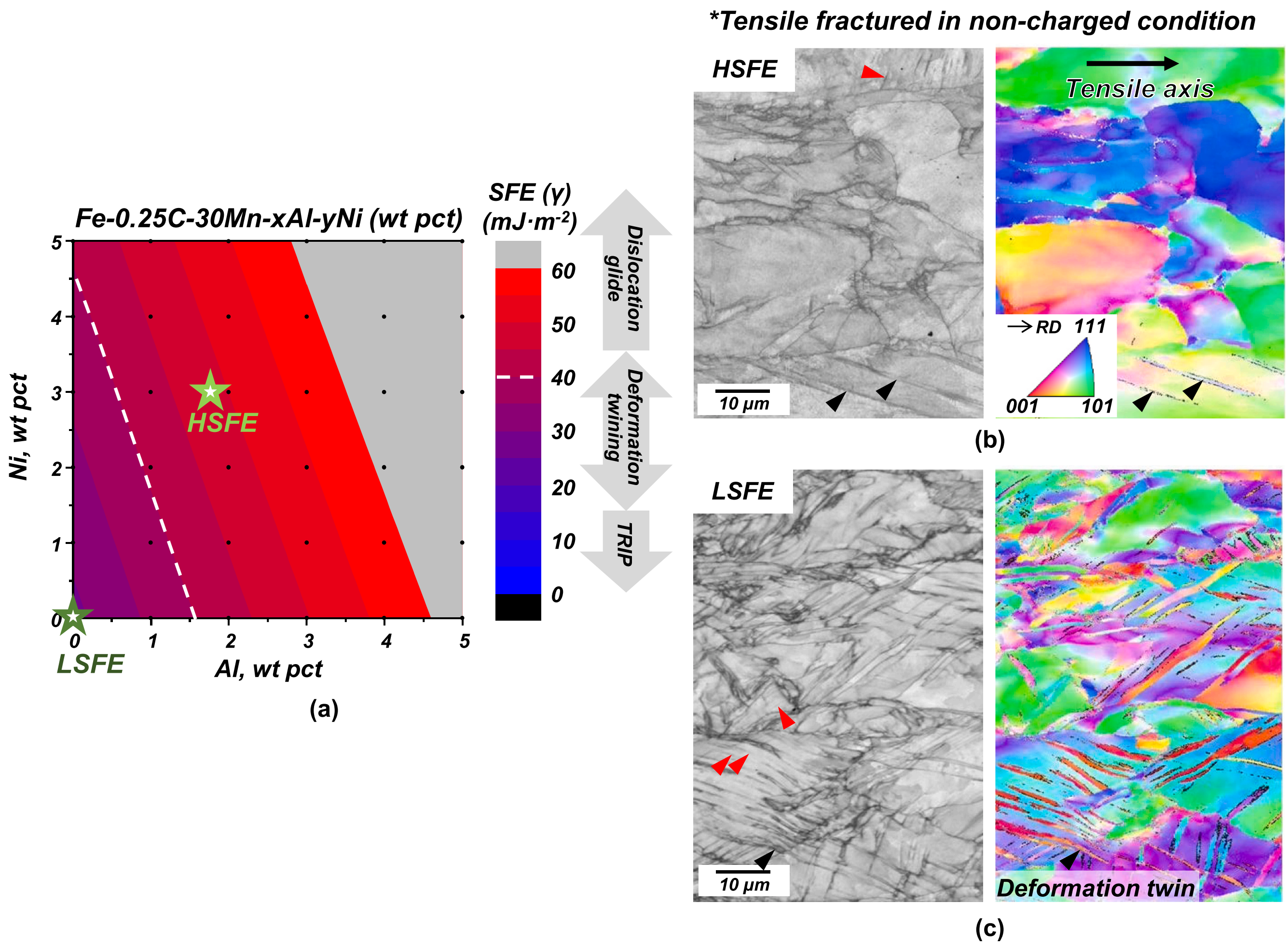

Fig. 2. SFE-dependent deformation mechanisms of the HSFE and LSFE alloys, evaluated through tensile testing in the non-charged condition. (a) Room temperature SFE map for an Fe-0.25C–30Mn-xAl-xNi (all in wt pct) austenitic alloy with varying Al and Ni concentrations. The calculated SFE values for the LSFE and HSFE alloys are indicated in (a). EBSD image quality (IQ) and inverse pole figure (IPF) maps for the deformed microstructures of the fractured specimens of (b) the HSFE and (c) LSFE alloys after tensile testing in air. In (b) and (c), the black and red arrowheads indicate deformation twins and thinner planar deformation structures, respectively. The HSFE and LSFE alloy tensile specimens fractured at engineering strains of 0.34 and 0.43, respectively.
(For interpretation of the references to colour in this figure legend, the reader is referred to the Web version of this article.)

Table 2
Notch tensile strength of high Mn austenitic alloys (LSFE and HSFE), evaluated through in-situ rising displacement testing in air and an electrochemical H charging environment using a 0.05 M NaOH aqueous solution and a 1.65 mA/cm^2 current density [12, 14].

Alloy	Notch Tensile Strength in Air (MPa)	Notch Tensile Strength in H Charging Environment (MPa)	Performance Ratio (Hydrogen/Air)
LSFE	854	755	0.89
HSFE	893	843	0.94

with respect to the loading axis, the HSFE alloys exhibited larger austenite lattice parameters, likely due to the alloying effects of Ni and Al. Compared to the LSFE alloy, the HSFE alloy, containing additional 1.75 wt % Al and 3.0 wt % Ni, showed a greater lattice parameter by approximately 1.0 x 10^{-3} nm as measured through neutron diffraction. In particular, Al is known to significantly increase the austenite lattice parameter [15,16]. H-precharging increased the lattice parameter by 0.03–0.08 % as shown in Fig. 5. The degree of increase in lattice strain was larger for the LSFE alloy. Overall, the reason for the different degrees of H-induced lattice expansion and strengthening between the two alloys is unclear and warrants further investigation.

In-situ neutron diffraction data collected during tensile testing were

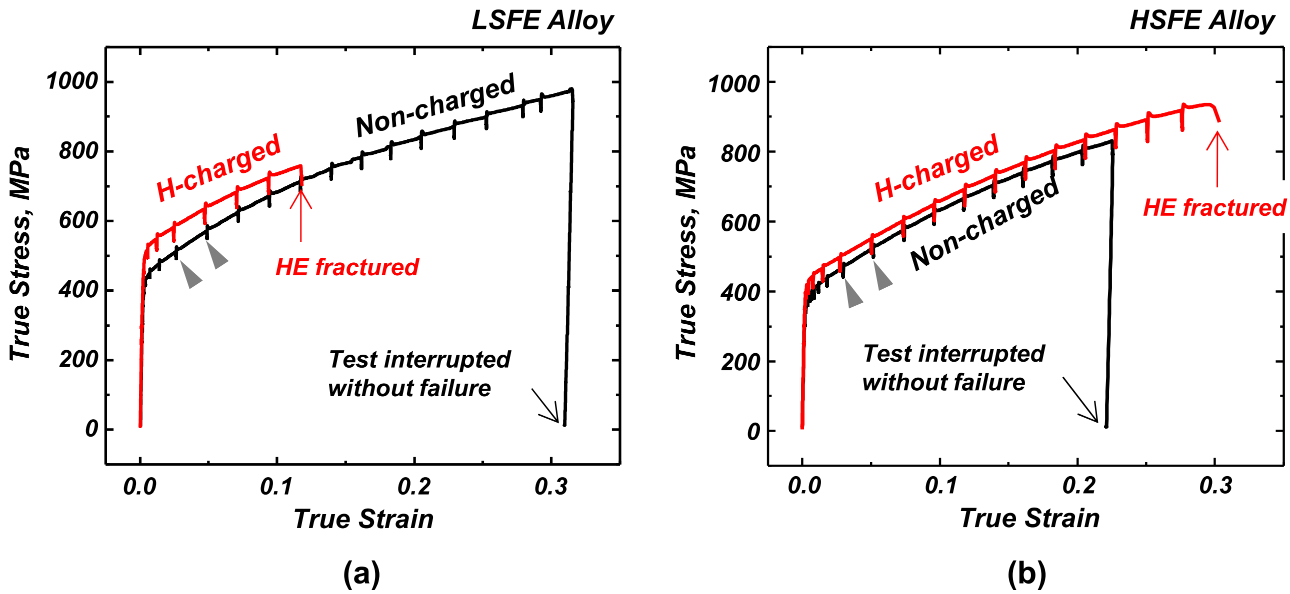

Fig. 3. True stress-true strain and curves for (a) the LSFE and (b) HSFE conditions in non-charged and H-precharged conditions, obtained during *in-situ* neutron diffraction measurements. Arrowheads in (a) and (b) indicate stress relaxation during holding for neutron diffraction measurements. The H-precharged conditions for both alloys were strained to failure, whereas the tensile tests for the non-charged conditions were interrupted before failure.

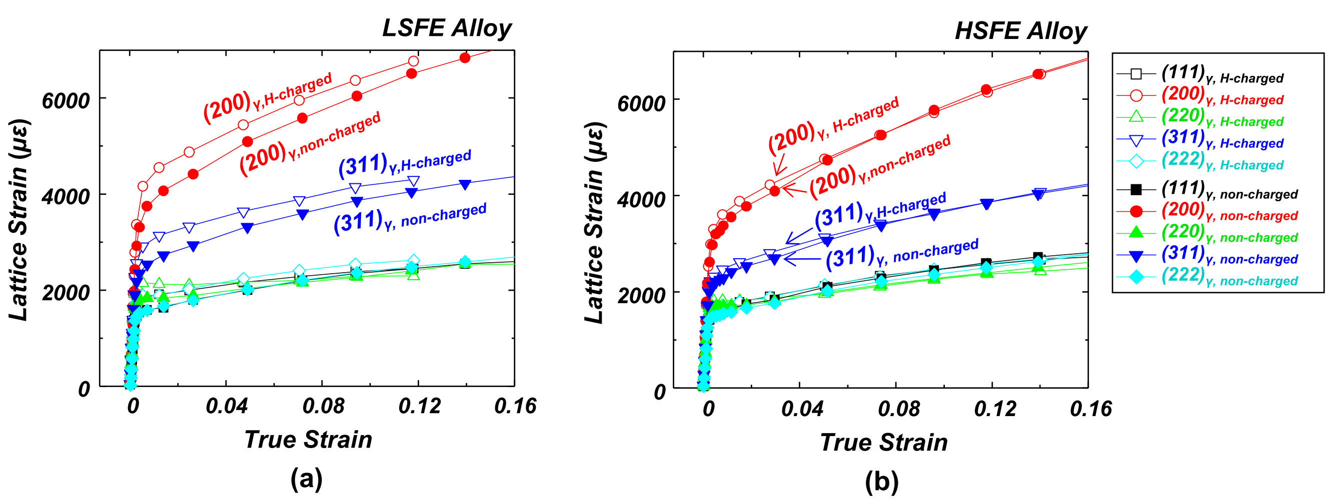

Fig. 4. Change in lattice strains of crystallographic planes along the axial direction (parallel to the tensile axis) due to H-precharging and tensile deformation for (a) the LSFE and (b) HSFE alloys, analyzed during *in-situ* neutron diffraction measurements during tensile testing of (a) the LSFE and (b) HSFE alloys.

used to quantitively analyze the H influence on the evolution of stacking fault frequency, relevant to the degree of planar slip behavior, in the LSFE and HSFE alloys. Fig. 6(a) shows the lattice strain for (111) and (222) planes as a function of applied true strain for the non-charged conditions of the two alloys. The same lattice strain data for the H-precharged conditions are also shown in Fig. 6(b). The deviation between the (111) and (222) lattice strains at a given strain indicates the formation of intrinsic stacking faults, as established in previous studies [17,18]. For the LSFE alloy, this deviation occurs at a lower strain in the H-precharged condition, i.e. at a true strain of 0.09, than in the non-charged condition (at a true strain of 0.025), implying that H accelerated the stacking fault frequency evolution. On the other hand, for the HSFE alloy in the non-charged condition, there was little difference between the (111) and (222) lattice strains at a given true strain level, suggesting an insignificant change in stacking fault density. This observation is consistent with the EBSD results (Table 1(a)) showing that the formation of deformation twins and stacking faults within the deformed microstructure was limited in the EBSD results of the HSFE alloy tested in the non-charged condition. In the H-precharged condition (Fig. 6(b)), the deviation of lattice strains was noted at a true strain of approximately 0.15, again confirming that H-charging facilitated stacking fault formation. Warren [19] proposed that the degree of the {nh,nk,nl} peak shift relative to {hkl} is proportional to the fraction of stacking faults on {hkl} planes. For FCC crystals, this relationship can be

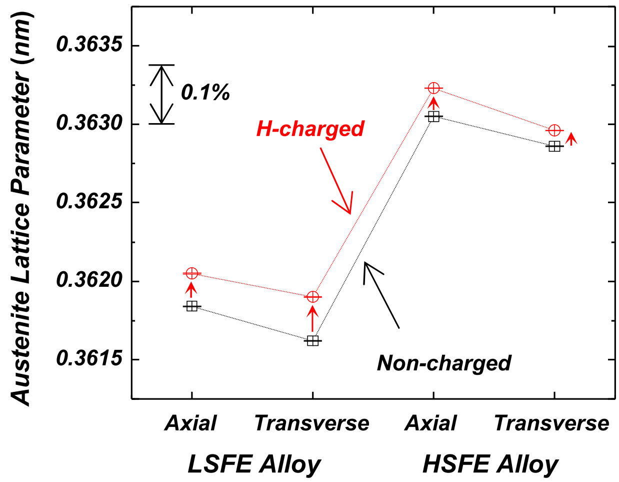

Fig. 5. Change in austenite lattice parameters due to H along the axial and transverse directions for the LSFE and HSFE alloys, measured through neutron diffraction.

expressed by the following equation, correlating the difference in (111) and (222) lattice strains with stacking fault probability (P_{SF}) [20]:

$$P_{SF} = \frac{32\pi}{3\sqrt{3}}\left[\left(\frac{\Delta d}{d_0}\right)222 - \left(\frac{\Delta d}{d_0}\right)111\right], \quad \text{Eq. 2}$$

where d_0 is the interplanar spacing before deformation and Δd is the change in interplanar spacing. P_{SF} represents the probability of encountering a stacking fault between any two layers in the FCC stacking sequence [21]. Fig. 6(c) shows the evolution of P_{SF} as a function of true strain for non-charged and H-precharged conditions of both alloys and confirms two key findings. First, H accelerates stacking fault formation in both the LSFE and HSFE alloys. Second, a higher SFE generally delays the onset of deformation-induced stacking fault formation to later stages of tensile straining in both non-charged and H-precharged conditions. Notably, in the H-precharged condition, both alloys fractured when the P_{SF} reached similar values of approximately 0.32–0.33, perhaps suggesting a critical role of stacking fault formation in H-assisted fracture processes.

Unexpectedly, negative P_{SF} values, beyond the range of measurement errors, were observed for the non-charged HSFE alloy. The origin of these negative values is not fully understood. However, similar observations [22–24] have been reported in previous neutron diffraction studies, and in these studies, negative PSF values were observed at low strain levels (below 0.1) or under conditions associated with relatively low stacking fault frequencies.

The effects of H and deformation on defect density were also inferred from peak broadening, quantified through full width at half maximum (FWHM) measurements using neutron diffraction data. Fig. 7 shows FWHM values for the LSFE and HSFE alloys in four different conditions: (i) non-charged, non-deformed, (ii) H-precharged, non-deformed, (iii) non-charged, deformed, and (iv) H-precharged, deformed conditions. The results shown in Fig. 7 were obtained from high-resolution diffraction measurements that involved a longer duration of data collection, and the details of the methodology are described in another published work [10]. Note also that for a given alloy condition, the specimens were deformed to a similar strain level in order to systematically compare the influence of H at a given deformation amount. That is, the H-precharged LSFE alloy fractured at a true stain of 0.12, and the non-charged condition was deformed to the same strain condition but did not fail. Similarly, for the HSFE alloy, the H-precharged and non-charged conditions either fractured at or deformed to comparable true stains of 0.32 and 0.33, respectively. In both alloy conditions, H charging had little influence on peak broadening in the non-deformed state, indicating negligible influence of H on initial defect density. Deformation resulted in significant increases in FWHM values as expected.

Interestingly, for the deformed condition, the H-precharged conditions exhibited more pronounced peak broadening compared to the non-charged conditions. This observation agrees with earlier investigations focused on Pd alloys, which showed that deformation in the presence of H accelerates dislocation density evolution [25]. Additionally, it was reported that H promoted twin formation and increased the density of geometrically necessary dislocations (GND) in single crystal 316L stainless steel [26]. In the non-deformed conditions here (Fig. 7), the LSFE alloy exhibited slightly higher FWHM values compared to the HSFE alloy. After deformation, the HSFE specimens had significantly higher FWHM values, indicating higher densities of dislocations and/or stacking faults, due to the higher strain levels of 0.32–0.33, compared to the LSFE specimens strained to 0.12. Notably, in the *in-situ* neutron diffraction results (Fig. 6), the two alloys exhibited similar stacking fault frequencies at their respective fracture strains in the H-precharged condition. These observations suggest that the more pronounced peak broadening for the HSFE specimen, compared to the LSFE specimen, is primarily attributed to an increase in dislocation density rather than stacking fault formation in accommodating deformation, even in the H-precharged condition.

The fractured specimens of the H-precharged alloys, analyzed using neutron diffraction, were characterized by EBSD (Fig. 8) and compared to specimens fractured in the non-charged condition (Fig. 2). The purpose of this analysis was to examine the critical deformation characteristics near the onset of fracture in non-charged and H-precharged conditions. The EBSD analysis focused on the cross-section of the region near the fracture surface, and the results are shown in Fig. 8. The black and red arrowheads in image quality (IQ) and IPF maps (Fig. 8) indicate deformation twins and thinner planar deformation structures (i.e. nano-sized twins or stacking faults). While the extent of planar slip behavior could not be quantitatively assessed, a comparison of IQ maps in Fig. 8 suggests relatively small differences in the quantities of planar

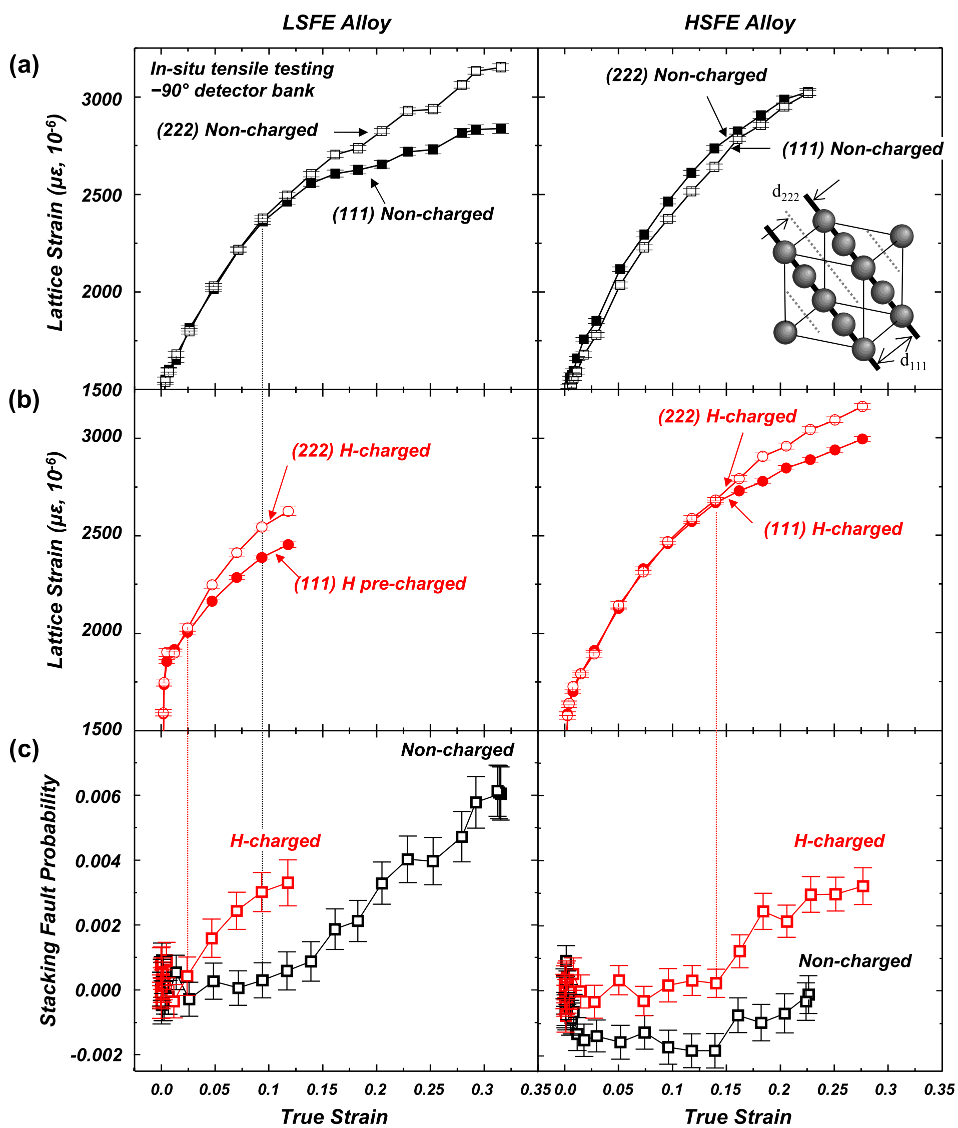

Fig. 6. Lattice strains of {111} and {222} crystallographic planes along the longitudinal direction (parallel to the tensile axis) and stacking fault probability for the LSFE (left) and HSFE (right) alloys in non-charged and H-precharged conditions as a function of true strain. (a) {111} and {222} lattice strains for the non-charged conditions. (b) {111} and {222} lattice strains for the H-precharged conditions. (c) Comparison of the stacking fault probability between the non-charged and H-precharged conditions. Black and red dashed lines indicate the points at which deviations between the (111) and (222) lattice strains are observed under non-charged and H-precharged conditions, respectively.
(For interpretation of the references to colour in this figure legend, the reader is referred to the Web version of this article.)

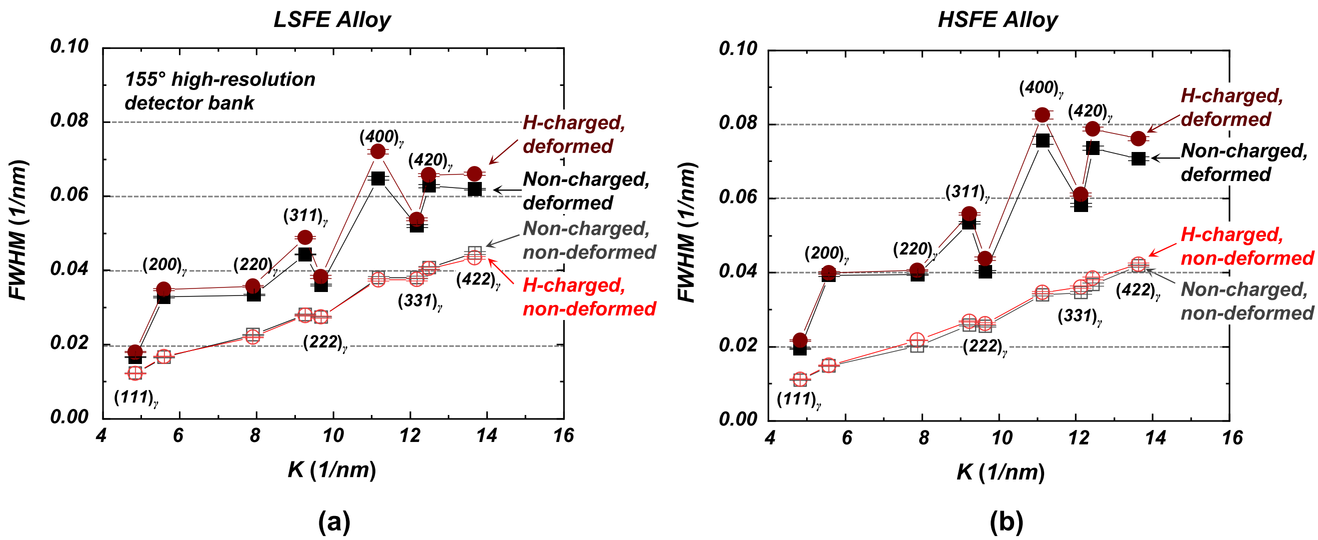

Fig. 7. Full width at half maximum (FWHM) values associated with austenite diffraction peaks as a function of diffraction vector K for (a) the LSFE and (b) HSFE alloys in non-charged and H-precharged conditions, measured during *ex-situ* neutron diffraction measurements using high-resolution detector bank in the SMARTS.

deformation structures between the two alloys. This observation is in clear contrast to the conditions of the specimens fractured in non-charged condition, where extensive planar slip behavior was observed exclusively in the LSFE alloy (compare Figs. 2 and 8). On the other hand, the HSFE specimen with high HE resistance exhibited a significantly higher average density of GND (4.7 x 10^{14} m^{-2}) than the LSFE specimen (2.5 x 10^{14} m^{-2}) (Fig. 8(c) and (f)), consistent with the more significant peak broadening observed for the HSFE alloy and higher strain level at the onset of fracture. Overall, it is interpreted that the evolution of planar deformation structures plays a more critical role than dislocation multiplication in promoting H-assisted fracture in H-precharged conditions.

In addition to SFE, grain size is known to influence deformation and HE mechanisms in austenitic steels. For example, Zan et al. [27] reported that grain refinement suppressed deformation twinning and enhanced HE resistance in an Fe–22Mn-0.6C (all in wt pct) twinning-induced plasticity (TWIP) steel. In the present study, the LSFE alloy, which exhibited a smaller *average* grain size than the HSFE alloy (Fig. 1), showed more pronounced deformation twinning and reduced HE resistance. It is therefore interpreted that, within the grain size range investigated, alloying-dependent SFE had a more significant influence on HE resistance. It should be noted, however, that the influence of bimodal grain size distributions on HE in FCC alloys is not yet well understood in the literature, and further investigation involving systematic variations of alloying and grain size will be needed to fully elucidate the role of microstructural factors, in combination with SFE, in deformation and HE mechanisms in austenitic steels.

4. Conclusions

The role of H on the deformation mechanisms in low (29 mJ/m^2) and high SFE (49 mJ/m^2) high Mn austenitic steels was evaluated through *in-situ* neutron diffraction during tensile loading. H charging increased yield and flow stress and caused some embrittlement (reduced ductility) during tensile straining of two high-Mn austenitic steels. The H-induced strengthening is attributed to solid solution strengthening via H-induced lattice distortion, which was less pronounced in the alloy with a higher SFE. H accelerates the evolution of defect densities, including dislocations and stacking faults, during deformation. The tendency to form planar deformation structures (deformation twins and stacking faults) relative to dislocations is suggested to play a critical role in promoting H-assisted fracture. The stacking fault frequency parameter, P_{SF}, obtained from neutron diffraction data, is an effective metric to quantify planar deformation and its correlation with HE sensitivity in austenitic steels. The higher SFE alloy exhibited greater resistance to HE, likely due to the reduced propensity to form stacking faults and twins during deformation in the H-precharged condition.

CRediT authorship contribution statement

Yuran Kong: Writing – review & editing, Writing – original draft, Visualization, Validation, Methodology, Investigation, Formal analysis, Data curation. **Pawan Kathayat:** Validation, Methodology, Investigation, Formal analysis, Data curation. **Alec Williamson:** Methodology, Investigation, Formal analysis, Data curation. **Donald W. Brown:** Writing – review & editing, Validation, Resources, Methodology, Investigation, Formal analysis, Data curation, Conceptualization. **Samantha K. Lawrence:** Resources, Methodology, Investigation, Formal analysis, Data curation, Conceptualization. **Bjørn Clausen:** Validation, Resources, Methodology, Investigation, Formal analysis, Data curation, Conceptualization. **Sven C. Vogel:** Resources, Methodology, Investigation, Formal analysis, Data curation. **Joseph A. Ronevich:** Writing – review & editing, Resources, Methodology, Investigation, Conceptualization. **Chris W. San Marchi:** Writing – review & editing, Validation, Resources, Methodology, Investigation, Formal analysis, Conceptualization. **Lucas Ravkov:** Validation, Methodology, Investigation, Formal analysis. **Levente Balogh:** Validation, Methodology, Investigation, Formal analysis. **John G. Speer:** Writing – review & editing, Validation, Supervision, Resources, Project administration, Methodology, Investigation, Funding acquisition, Formal analysis, Conceptualization. **Kip O. Findley:** Writing – review & editing, Validation, Supervision, Resources, Project administration, Methodology, Investigation, Funding acquisition, Formal analysis, Conceptualization. **Lawrence Cho:** Writing – review & editing, Writing – original draft, Visualization, Validation, Supervision, Resources, Project administration, Methodology, Investigation, Formal analysis, Data curation,

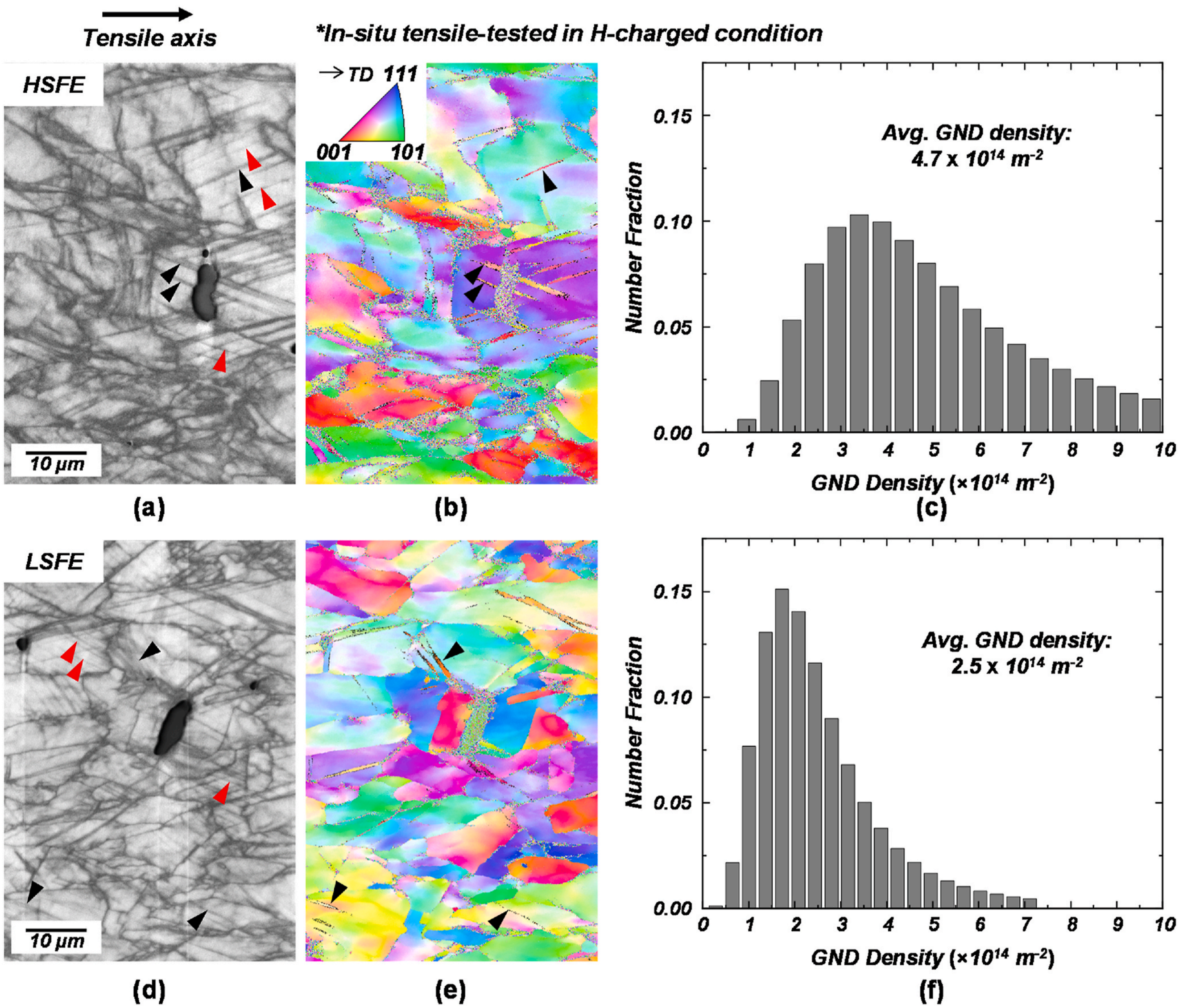

Fig. 8. EBSD results for the deformed microstructures of the fractured specimens of the HSFE ((a) to (c)) and LSFE alloys ((d) to (e)) after *in-situ* tensile testing in H-precharged conditions. EBSD (a,d) IQ maps and (b,d) IPF maps of the deformed microstructures of the fractured specimens and (c,f) corresponding geometrically necessary dislocation (GND) density histograms. In the EBSD IQ and IPF maps, black and red arrowheads indicate deformation twins and thinner planar deformation structures (e.g., nano-sized twins or stacking faults), respectively. The LSFE and HSFE alloy tensile specimens fractured at true strains of 0.12 and 0.32, respectively. (For interpretation of the references to colour in this figure legend, the reader is referred to the Web version of this article.)

Conceptualization.

Declaration of competing interest

The authors declare that they have no known competing financial interests or personal relationships that could have appeared to influence the work reported in this paper.

Acknowledgements

The authors gratefully acknowledge the support from the US DOE Hydrogen and Fuel Cells Technology Office (HFTO) and H2@Scale program, under award number DE-EE0008828. The authors also acknowledge the support of the sponsors of the Advanced Steel Processing and Products Research Center (ASPPRC) at the Colorado School of Mines. The authors greatly appreciate the support of POSCO for providing and processing the materials used for this investigation. This article has been authored by an employee of National Technology & Engineering Solutions of Sandia, LLC under Contract No. DE-NA0003525 with the U.S. Department of Energy (DOE). The employee owns all right, title and interest in and to the article and is solely responsible for its contents. The United States Government retains and the publisher, by accepting the article for publication, acknowledges that the United States Government retains a non-exclusive, paid-up, irrevocable, world-wide license to publish or reproduce the published form of this article or allow others to do so, for United States Government purposes. The DOE will provide public access to these results of federally sponsored research in accordance with the DOE Public Access Plan https://www.energy.gov/downloads/doe-public-access-plan. This paper describes objective technical results and analysis. Any subjective views or opinions that might be expressed in the paper do not necessarily represent the views of the U.S. Department of Energy or the United States Government.

Appendix A. Supplementary data

Supplementary data to this article can be found online at https://doi.org/10.1016/j.ijhydene.2025.06.023.

References

[1] Gibbs PJ, Hough PD, Thürmer K, Somerday BP, San Marchi C, Zimmerman JA. Stacking fault energy based alloy screening for hydrogen compatibility. J Occup Med 2020;72:1982–92.
[2] Castañeda JA, Zambrano OA, Alcázar GA, Rodríguez SA, Coronado JJ. Stacking fault energy determination in fe-mn-al-c austenitic steels by x-ray diffraction. Metals 2021;11(11):1701.
[3] Michler T, San Marchi C, Naumann J, Weber S, Martin M. Hydrogen environment embrittlement of stable austenitic steels. Int J Hydrogen Energy 2012;37(21):16231–46.
[4] Koyama M, Akiyama E, Lee Y-K, Raabe D, Tsuzaki K. Overview of hydrogen embrittlement in high-Mn steels. Int J Hydrogen Energy 2017;42(17):12706–23.
[5] Koyama M, Akiyama E, Tsuzaki K, Raabe D. Hydrogen-assisted failure in a twinning-induced plasticity steel studied under in situ hydrogen charging by electron channeling contrast imaging. Acta Mater 2013;61(12):4607–18.
[6] Koyama M, Okazaki S, Sawaguchi T, Tsuzaki K. Hydrogen embrittlement susceptibility of Fe-Mn binary alloys with high Mn content: effects of stable and metastable ε-martensite, and Mn concentration. Metall Mater Trans A 2016;47:2656–73.
[7] Zhou X, Skelton R, Sills R, San Marchi C. Slip transmission and voiding during slip band Intersections in Fe70Ni10Cr20 stainless steel. Scripta Mater 2022;220:114925.
[8] Nibur K, Bahr D, Somerday B. Hydrogen effects on dislocation activity in austenitic stainless steel. Acta Mater 2006;54(10):2677–84.
[9] Sabisch J, Sugar JD, Ronevich J, San Marchi C, Medlin DL. Interrogating the effects of hydrogen on the behavior of planar deformation bands in austenitic stainless steel. Metall Mater Trans A 2021;52:1516–25.
[10] Cho L, Kong Y, Kathayat P, Brown DW, Lawrence SK, Clausen B, Vogel SC, Ravkov L, Balogh L, Ronevich JA. Influence of hydrogen on deformation and embrittlement mechanisms in a high Mn austenitic steel: in-Situ neutron diffraction and diffraction line profile analysis. Acta Mater 2024;281:120420.
[11] Saeed-Akbari A, Imlau J, Prahl U, Bleck W. Derivation and variation in composition-dependent stacking fault energy maps based on subregular solution model in high-manganese steels. Metall Mater Trans A 2009;40:3076–90.
[12] Kathayat P. Microstructural engineering of Mn alloyed austenitic steel for hydrogen storage and delivery, M.S. Thesis. Golden, CO: Colorado School of Mines; 2023.
[13] De Cooman BC, Estrin Y, Kim SK. Twinning-induced plasticity (TWIP) steels. Acta Mater 2018;142:283–362.
[14] Cho L, Marchi CS, Kong Y, Ronevich J, Kathayat P, Speer J, Kosberg A, Findley K. Microstructural engineering of high manganese steels for hydrogen storage and delivery. Paper presented at the AMPP annual conference + expo, Denver, CO. 2023. p. 19453.
[15] Lehnhoff G, Findley K, De Cooman B. The influence of silicon and aluminum alloying on the lattice parameter and stacking fault energy of austenitic steel. Scripta Mater 2014;92:19–22.
[16] Babu SS, Specht ED, David SA, Karapetrova E, Zschack P, Peet M, Bhadeshia H. In-situ observations of lattice parameter fluctuations in austenite and transformation to bainite. Metall Mater Trans A 2005;36:3281–9.
[17] Jeong J, Woo W, Oh K, Kwon S, Koo Y. In situ neutron diffraction study of the microstructure and tensile deformation behavior in Al-added high manganese austenitic steels. Acta Mater 2012;60(5):2290–9.
[18] Neding B, Tian Y, Ko JP, Hedström P. Correlating temperature-dependent stacking fault energy and in-situ bulk deformation behavior for a metastable austenitic stainless steel. Mater Sci Eng A 2022;832:142403.
[19] Warren BE. X-Ray diffraction. Courier Corporation 1990.
[20] Kang M, Woo W, Lee Y-K, Seong B-S. Neutron diffraction analysis of stacking fault energy in Fe–18Mn–2Al–0.6 C twinning-induced plasticity steels. Mater Lett 2012;76:93–5.
[21] He H, Naeem M, Zhang F, Zhao Y, Harjo S, Kawasaki T, Wang B, Wu X, Lan S, Wu Z. Stacking fault driven phase transformation in CrCoNi medium entropy alloy. Nano Lett 2021;21(3):1419–26.
[22] Saleh AA, Pereloma EV, Clausen B, Brown DW, Tomé CN, Gazder AA. Self-consistent modelling of lattice strains during the in-situ tensile loading of twinning induced plasticity steel. Mater Sci Eng A 2014;589:66–75.
[23] Liu S, Gao H, Wei D, Kong C, Kumara L, Fu M, Yu H. Deformation mechanism of a metastable medium entropy alloy strengthened by the synergy of heterostructure design and cryo-pre-straining. Int J Plast 2024;183:104162.
[24] Cai B, Liu B, Kabra S, Wang Y, Yan K, Lee PD, Liu Y. Deformation mechanisms of Mo alloyed FeCoCrNi high entropy alloy: in situ neutron diffraction. Acta Mater 2017;127:471–80.
[25] Chen Y, Barth HP, Deutges M, Borchers C, Liu F, Kirchheim R. Increase in dislocation density in cold-deformed Pd using H as a temporary alloying addition. Scripta Mater 2013;68(9):743–6.
[26] León-Cázares FD, Zhou X, Kagay B, Sugar JD, Alleman C, Ronevich J, San Marchi C. Hydrogen effects on the deformation and slip localization in a single crystal austenitic stainless steel. Int J Plast 2024;180:104074.
[27] Zan N, Ding H, Guo X, Tang Z, Bleck W. Effects of grain size on hydrogen embrittlement in a Fe-22Mn-0.6 C TWIP steel. Int J Hydrogen Energy 2015;40(33):10687–96.